CrossMark

Identifying Impact Melt from the Smythii Basin: Toward an Improved Chronology for Lunar Basin Formation

Kirby D. Runyon[1] , Lyle Nelson[2] , and Daniel P. Moriarty III[3]

[1] Planetary Exploration Group, Johns Hopkins APL, 11101 Johns Hopkins Road, Laurel, MD 20723, USA; kirby.runyon@jhuapl.edu
[2] Department of Earth and Planetary Sciences, Johns Hopkins University, Baltimore, MD, 21218, USA
[3] USRA and NASA Goddard Space Flight Center, Planetary Geodynamics Laboratory, Code 698, Greenbelt, MD 20771, USA

Abstract

At c. 820 km in diameter, the Smythii impact basin is one of the large lunar basins (>200 km diameter) thought to have formed during the pre-Nectarian period. We combine Lunar Reconnaissance Orbiter imagery, topography, and Moon Mineralogy Mapper compositional data to interpret the surface and subsurface geology of the Smythii basin with the goal of identifying datable impact melt for investigation by a future lunar lander. Surface outcrops exposed on the central peak of the Schubert C crater are identified as uplifted deposits of Smythii impact melt, and a mission concept is presented for sampling these exposures in order to establish the absolute age of the Smythii basin using radioisotopic geochronology. This mission concept is in line with one of the current top-tier priorities for lunar science: determining the age of large basins and thus constraining the impact flux during the Moon's first billion years, which is a proxy record for the role of impacts on the surface environment and habitability of early Earth and the inner solar system during this interval.

Unified Astronomy Thesaurus concepts: Lunar impacts (958); The Moon (1692); Lunar geochronology (954); Isotopic abundances (867); Lunar craters (949); Selenology (1441); Lunar surface (974); Lunar mineralogy (962); Lunar petrology (967)

1. Introduction

During Earth's first billion years, life emerged on its surface (e.g., Knoll et al. 2016; Pearce et al. 2018). The earliest convincing lines of evidence for life on Earth come from the oldest preserved low-grade metasedimentary rocks, which are c. 3.5–3.4 Ga, and include biogenic textures within stromatolites (e.g., van Kranendonk et al. 2003) and biologically consistent carbon and sulfur isotope fractionation patterns (e.g., Tice & Lowe 2006; Bontognali et al. 2012). The occurrences of ^{13}C-depleted carbonaceous material in c. 3.8–3.7 Ga metamorphic rocks (Mojzsis et al. 1996; Rosing 1999) and in 4.1 Ga zircon grains (Bell et al. 2015) are suggestive of still older biological processes but are not definitive evidence for life in the Hadean or early Archean because abiotic processes are also capable of generating the observed values (e.g., McCollom et al. 2010). While the precise mechanisms and environments for Earth's Hadean(?)–Archean abiogenesis remain unknown (e.g., Joyce 2002), it is critical to understand how planetary impact events disrupted, altered, and otherwise defined life's earliest habitats on Earth.

Most of Earth's geologic record of this time period has been removed by the operation of active tectonics and erosion during the ensuing 3.5 billion years. However, the temporally correlative geologic record of the Moon is largely intact. Among all of the solar system's planets, the earliest geologic histories of Earth and the Moon are uniquely linked. The emerging view of the Moon's first billion years suggests a declining impact flux and that the Moon's large basins (>200 km) were formed during this time (e.g., Spudis et al. 2011; Fassett et al. 2012; Michael et al. 2018; Orgel et al. 2018). This

hypothesis of gradual decline stands in contrast to the Terminal Lunar Cataclysm hypothesis (Tera et al. 1974), which proposed a significant spike in basin formation between 3.8 and 4.0 Ga, known as the Late Heavy Bombardment (e.g., Kring & Cohen 2002; Morbidelli et al. 2018). The interpretation of a relatively brief surge in impact flux and basin formation may have stemmed from sample bias, given that Apollo-era sample collection was restricted to <4% of the lunar surface (Warren 2003); it is likely that many of the age-determined impact melt samples from Apollo and Luna date the formation of the Imbrium basin at 3.9 Ga and that only the Imbrium-forming event has been dated with certainty (Cadogan et al. 1977; Stettler & Albarede 1978; Swindle et al. 1991; Haskin 1998; Chapman et al. 2007; Norman et al. 2010; Liu et al. 2012, 2012; Merle et al. 2014; Cohen et al. 2018; van der Bogert et al. 2017). Additionally, modeling has suggested that apparent clusters of $^{40}Ar/^{39}Ar$ ages from lunar samples could be a misleading result of the diffusive loss of ^{40}Ar within a monotonically declining impact flux (Boehnke & Harrison 2016). The continuing uncertainty in the time span for the Moon's heavy bombardment is problematic because the temporal distribution of large basin formation on the Moon is used as a proxy for the impact flux on Earth during this same interval. If the large number of preserved lunar impacts at the basin scale is an accurate reflection of the impact flux on Earth, those impacts would have profoundly influenced the surface environment and habitability of early Earth.

Identifying, sampling, and determining the age of impact melt deposits confidently linked to a basin or crater is thus a top-tier priority for lunar science (e.g., National Research Council 2007). Establishing a precise and absolute lunar basin chronology is the only way to discriminate among various hypotheses for inner solar system heavy bombardment, such as the sawtooth versus smooth, monotonic decline scenarios for lunar impactor flux (e.g., Morbidelli et al. 2012, 2018).

Identifying exposed impact melt deposits for the Moon's largest basins where possible is a necessary first step before sampling and age determination can occur, and this must be done systematically for each basin. During central peak formation, subsurface material is uplifted from depth according to well-constrained scaling laws (Cintala & Grieve 1994, 1998). And, the uplift process may not reset radioisotopic ages for many isotope systems: Young et al. (2013, 2016) dated samples from in and around Canada's Mistastin impact structure using the (U–Th)/He method, a low-temperature thermochronologic method analogous to the low-temperature $^{40}Ar/^{39}Ar$ commonly used for lunar samples. They found the ages of Mistastin's central peak lithologies and rocks external to Mistastin to be comparable, showing that ages in the central peak are not reset during crater formation (Young et al. 2013, 2016) and can thus date units superposed by complex craters. Applying this philosophy to the Moon, the central peak of the Yerkes crater likely exposes relatively pristine, only lightly shocked impact melt from the superimposed Crisium basin, which could reveal the age of this large basin (Runyon et al. 2020). Another prominent large basin is the Smythii basin, located on the Moon's eastern near-side–far-side boundary. The Smythii basin's relative age is pre-Nectarian (Wilhelms & McCauley 1971; Spudis et al. 2011) and shows substantial degradation and younger, superposed craters. For this special issue of *The Planetary Science Journal*, we identify candidate Smythii impact melt exposures where the melt sheet may have been uplifted within the central peaks of superposed craters. We accomplish this via geologic mapping, compositional analyses, and geologic cross-section interpretation. Finally, we present a mission concept to sample outcrops of candidate Smythii impact melt that are exposed on the central peak of Schubert C.

2. Methods

2.1. Compositional Interpretation

Moon Mineralogy Mapper (M^3; Pieters et al. 2009) data provide the highest-spectral-resolution mineralogical data available for the lunar surface and are therefore ideally suited for characterizing compositional diversity. For these analyses, we use Planetary Data System (PDS)–released Level 2 global-mode M^3 reflectance images, which have been thermally and photometrically corrected and normalized to a standard viewing geometry ($i = 30°$, $e = 0°$, $g = 30°$) (Besse et al. 2013). These data have a nominal spatial resolution of 140–280 m per pixel and a spectral resolution of 20–40 nm per channel from 540–3000 nm (Pieters et al. 2009; Boardman et al. 2011).

Spectral variations across the lunar surface are dominated by differences in the abundance and composition of pyroxenes. Therefore, differences in mineralogy across the Smythii basin are well captured by differences in reflectance and the diagnostic properties (depth and center) of the 1 μm and 2 μm absorption bands. To first order, absorption-band depths increase with pyroxene abundance, although factors such as optical maturity also affect band depths (Burns 1993). Band centers are sensitive to pyroxene composition. Mg-rich pyroxenes exhibit short-wavelength 1 μm and 2 μm bands; band centers shift to longer wavelengths with increasing Fe and Ca content (Klima et al. 2007, 2011; Moriarty & Pieters 2016).

Maps of these mineralogically sensitive parameters (1 and 2 μm absorption-band depths and centers) were generated from M^3 data using the Parabolas and two-part Linear Continuum (PLC) method, which was developed and validated for use with M^3 data by Moriarty & Pieters (2016). The PLC approach performs parabola fits to the 1 μm and 2 μm absorption bands after a two-part linear continuum is calculated (from three tie points) and removed. The code is optimized to derive detailed mineralogical information from M^3 images while minimizing the contribution of instrument artifacts. Several mineralogically sensitive parameters are derived from these parabola fits. The 1 and 2 μm band centers are sensitive to pyroxene composition, as described above. Similarly, the 1 and 2 μm band depths are sensitive to mafic abundance. We also employ a secondary measure of measuring band depth that does not rely on parabola fitting, which can fail for noisy or low-mafic spectra. The integrated band depth measures the total area of the 1 and 2 μm absorption bands by taking the sum of the depths of each wavelength channel across each continuum-removed absorption band then multiplying each depth by the bandwidth. The resulting suite of six spectral parameters (1 and 2 μm band depth, band center, and integrated band depth) provides a robust overview of the regional mineralogical diversity. For most common lunar materials, the 1 and 2 μm band depths and centers vary in concert. However, the 1 and 2 μm bands exhibit divergent behavior for less-common materials such as ilmenite, volcanic glasses, pure olivine, pure spinel, and pure crystalline plagioclase (Isaacson et al. 2011; Cheek et al. 2013; Pieters et al. 2014; Moriarty & Pieters 2016).

Regional analyses of the Smythii basin were performed with PLC-generated parameter maps of band depth and center derived from M^3 global mosaics produced by Boardman et al. (2011). These 1 km pixel^{-1} mosaics have a $10\times$ lower spatial resolution than full-resolution global-mode M^3 data but a higher signal-to-noise ratio. Detailed local analyses of Neper, Schubert C, and Haldane were performed with the M^3 image M3G20090602T074711. After parameter maps were generated using the PLC technique (implemented in IDL), M^3 images were georeferenced (using the M^3 L1B location file backplanes available on the PDS) for integration with other lunar remote-sensing data in ArcMap 10.

Lemelin et al. (2016) describe the derivation of the Kaguya Multiband Imager plagioclase abundance in weight fraction and produced ready-to-use, near-global maps of plagioclase abundance (among other minerals). This product has a spatial resolution of 59 m per pixel and is available through the USGS and LROC Quickmap (https://astrogeology.usgs.gov/search/map/Moon/Kaguya/MI/MineralMaps/Lunar_Kaguya_MIMap_MineralDeconv_PlagioclasePercent_50N50S). These parameter maps were used to evaluate the mineralogical diversity across the region and to characterize the compositional properties of candidate impact melt materials. Parameter maps are also useful for identifying areas of interest for more detailed spectral characterization (Figures 2–6).

2.2. Geologic Mapping and Cross-section Interpretation

A detailed surface geologic mapping of the Smythii basin was conducted using imagery and topographic data from the Lunar Reconnaissance Orbiter Camera (LROC) and Lunar Orbiter Laser Altimeter (LOLA) combined with the M^3 (Pieters et al. 2009) hyperspectral images and Kaguya Multiband Imager plagioclase abundance maps (Lemelin et al. 2016). The surface geology, composition, and topography data, along with principles of lunar impact geology, were implemented to
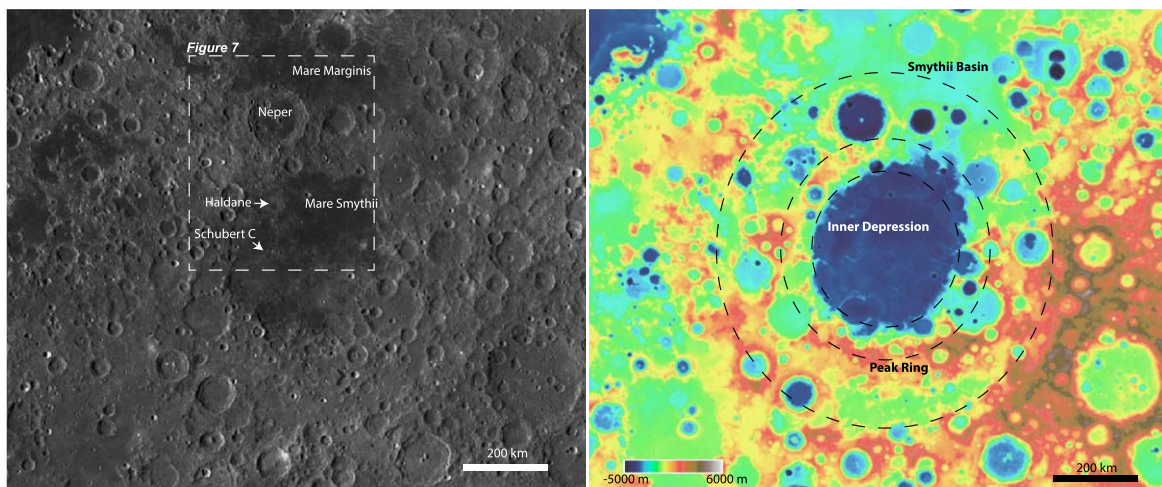
Figure 1. Location map of the Smythii basin on the Moon's eastern near-side–far-side boundary, including the superposed complex craters investigated herein (LROC/WAC base map from QuickMap; centered near 0°N, 86°E). GLD100(+LOLA) topographic map of the Smythii basin with interpretations of c. 820 km diameter basin rim, c. 510 km diameter peak ring, and c. 360 km diameter inner depression. Equidistant cylindrical projections from QuickMap used in both.

interpret the subsurface geology of the Smythii basin with the goal of identifying probable surface outcrops of uplifted Smythii impact melt. Outcrops of impact melt serve as potential locations for targeted sampling by a future lunar surface mission with the objective of determining the age of impact melt from the formation of the Smythii basin with radioisotopic geochronology. Images from the LROC Wide-Angle Camera (WAC) were used to map at 1:40,000 scale across the entire map area (allowing a pixelated view of the 100 m pixel^{-1} data), while images from the LROC narrow-angle cameras (NAC) were used for more detailed mapping of specific target areas (<2 m pixel^{-1}), including the Neper, Schubert C, and Haldane craters and their central peaks. Topographic elevation data were extracted from the Global Lunar Digital Terrain Model (GLD100), which was produced using WAC stereo image data with a pixel spacing of 100 m and referenced to LOLA (Scholten et al. 2012).

Geologic map interpretations were completed using QGIS software and informed by LROC WAC and NAC imagery, terrain data from GLD100, and composition data from M^3 hyperspectral images and Kaguya Multiband Imager mineral abundance maps (described below). Using the interpreted surface geology map and terrain data, the subsurface geology was interpreted along a cross section of c. 490 km extending from Mare Marginis to the north of the Smythii basin and outside of its crater wall, to the interior of the Smythii basin through three younger complex impact craters: Neper, Schubert C, and Haldane. Interpretation of the subsurface geology at 5× vertical exaggeration was informed by lunar geological principles, including scaling rules relating the complex crater diameter to the depth of the central peak uplift (Cintala & Grieve 1998).

Here, we give our description of map units. Mare: Low reflectance, sparse cratering/smooth surface texture, low topographic slope relatively undifferentiated; may embay topographic features. Lunar swirl: Irregular surficial patches of higher-reflectance, usually mare material; also identified in Denevi et al. (2016). Smythii impact melt: Intrabasin plains of heavily cratered, high-reflectance highland material located between Smythii's interpreted inner ring and basin rim. Degraded Smythii melt: Mixture of high- and low-reflectance material; cratered, cracked, at locations embayed by mare;

interior to the interpreted Smythii inner ring. Craters into Smythii Melt: Craters larger than 15 km diameter superposing interpreted Smythii melt. Smythii basin: All geologic units interior to the interpreted outer ring of the Smythii basin. Craters into Smythii basin: Craters larger than 15 km diameter superposing any part of the Smythii basin. Neper wall material: Portion of Neper crater from rim to the mare fill; faulted in places. Neper ejecta: Circum-Neper deposit appearing slightly elevated relative to surrounding plains with occasional lobate deposits near its distal ends.

3. Results and Discussion

The Smythii basin is one of ∼30 lunar basins interpreted to be pre-Nectarian in age due to its highly degraded surface expression (e.g., Wilhelms & McCauley 1971; Spudis et al. 2011). The floor of the Smythii basin features a highlands floor with partial mare basalt fill, floor-fractured craters (implying the presence of subsurface magmatic dikes), rilles, pyroclastic deposits, cryptomare deposits around craters, ejecta from the Crisium basin to the west, and evidence for tectonic deformation (Wilhelms & El-Baz 1977; Yingst & Head 1998; Gillis & Spudis 2000). Hiesinger et al. (2010) used crater statistics to date the basalts of Mare Smythii to 3.14–3.48 Gyr old, constraining the end of intrabasin volcanism here. In this study, the outer rim of the Smythii basin is interpreted with high confidence to the south using topographic data from the GLD100 DEM and lower confidence to the north where the topography has been degraded by younger craters and the basin rim has been buried beneath flood basalts of Mare Marginis (Figure 1). A distinct peak ring is identified based on topographic data from the southern part of the Smythii basin and extrapolated to the northern part of the basin. The central depression of the basin is readily apparent from topographic data with a diameter of c. 360 km and is partially filled in by flood basalt of Mare Smythii (Figure 1). The interpretation of the position of the Smythii basin and its features based on topographic signatures used herein is consistent with interpretation based on the residual Bouguer gravity anomaly extracted from observations of the Gravity Recovery and Interior Laboratory (GRAIL) mission (Neumann et al. 2015). Thus, the inferred diameter of the Smythii basin is c. 820 km as
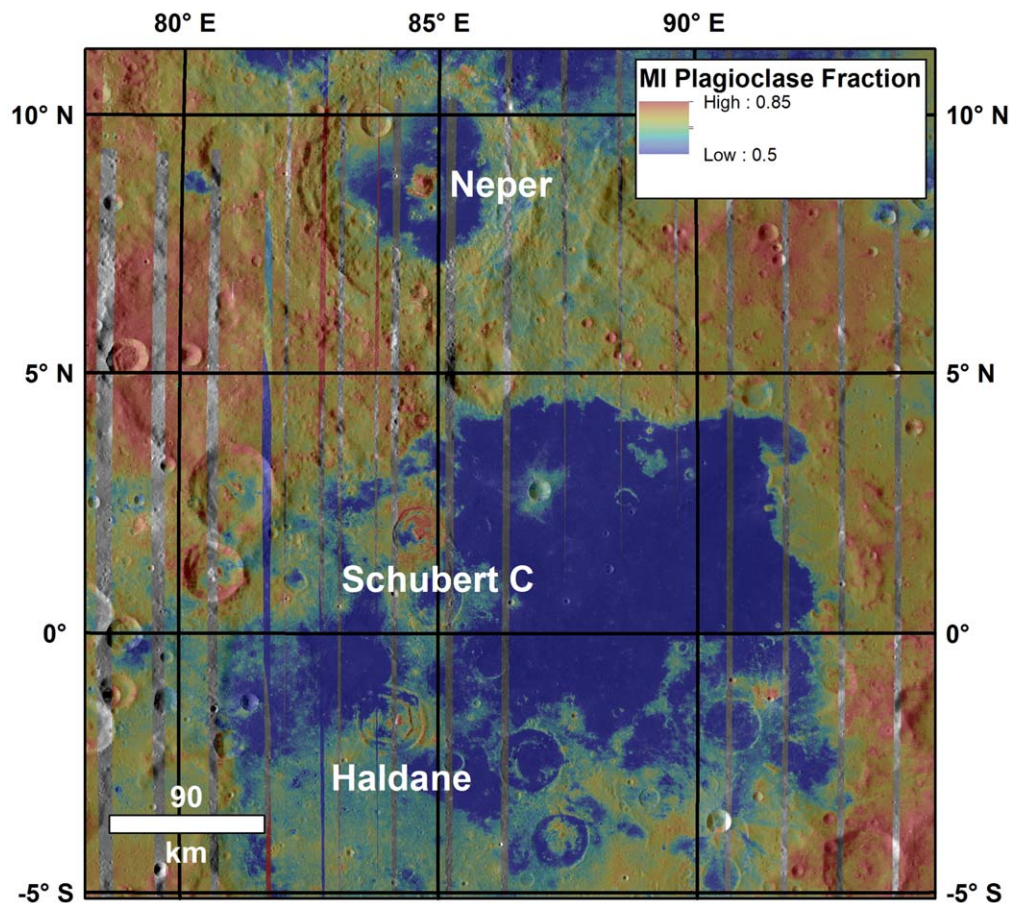
Figure 2. Kaguya Multiband Imager plagioclase abundance data (in weight fraction) for the Smythii region, including craters Haldane, Schubert C, and Neper (Lemelin et al. 2016). Mare basalts exhibit relatively low plagioclase abundance (∼35 wt%), while feldspathic crustal materials exhibit high plagioclase abundance.

measured from the widest apparent topographic rim and similar to the 840 km reported by Wilhelms et al. (1987).

Estimates of the extent and thickness of the Smythii basin's central impact melt sheet can be informed through comparisons with the similarly sized Orientale basin, where flooding by mare basalts and degradation by superposed craters were less extensive and thus impact melt facies are more readily observed (e.g., Head 1974). (However, analogizing the Smythii and Orientale basins with each other is not strictly a "one-to-one" comparison. The Orientale basin-forming impact was oblique and occurred on a topographic boundary, resulting in asymmetrical distribution of ejecta and impact melt (e.g., Morse et al. 2018). It is not currently possible to determine for sure if the Smythii impact event was oblique due to the obliterated rings in the north and lack of preserved ejecta, but the Smythii basin did not form on a topographic boundary like the Orientale basin.) The 364 km diameter (Neumann et al. 2015) inner depression within Orientale (interior to the Inner Rook Ring) has been suggested to result in part from vertical contraction of the impact melt sheet due to melt cooling and crystallization (Bratt et al. 1985; Wilson & Head 2011; Vaughan et al. 2013). Gravity measurements from GRAIL suggest a melt-sheet thickness of up to c. 10–11 km thick (Zuber et al. 2016), somewhat thicker than the maximum estimated thickness in the central part of the basin of up to 9 km (Spudis et al. 2014). Stratigraphic relationships suggest that the melt sheet of the Orientale basin thins to c. 6 km near the inner Rook ring (Spudis et al. 2014); melt deposit thicknesses of the

same order would be reasonable to expect for the Smythii basin.

An inner ring analogous to that of the Orientale basin is observed within the Smythii basin. The inner ring within Smythii is c. 360 km in diameter (or c. 375 km; Neumann et al. 2015), similar to that of Orientale (the interior of which is mapped as degraded Smythii melt). At c. 438 km in diameter, Smythii's Bouguer anomaly is also essentially identical in size to the 436 km Bouguer anomaly of Orientale (Neumann et al. 2015). The similarly sized Bouguer anomalies may imply comparable excavated volumes of material, including impact melt. If that is the case, then we would expect the Smythii impact event to have produced a melt sheet similar in thickness. Therefore, it is likely that Smythii is host to an impact melt sheet c. 10 km thick toward the middle, thinning to perhaps c. 6 km toward the massifs along the inner ring (Spudis et al. 2014). Analogous to the zones of impact melt and breccia beyond the inner massif ring of Orientale basin (Osinski et al. 2011), splashed melt, mixed with impact breccia and ejecta, was likely emplaced in the annulus of the Smythii basin between the peak ring(s) and the basin wall, but it likely is significantly thinner than that underlying the central region and more likely to be mixed with slumped material from the peak ring and basin wall.

Characterizing the mineralogical diversity of the Smythii basin in geologic context provides insight into the evolution and stratigraphy of the basin. We evaluate the mineralogy of Smythii using Kaguya Multiband Imager plagioclase
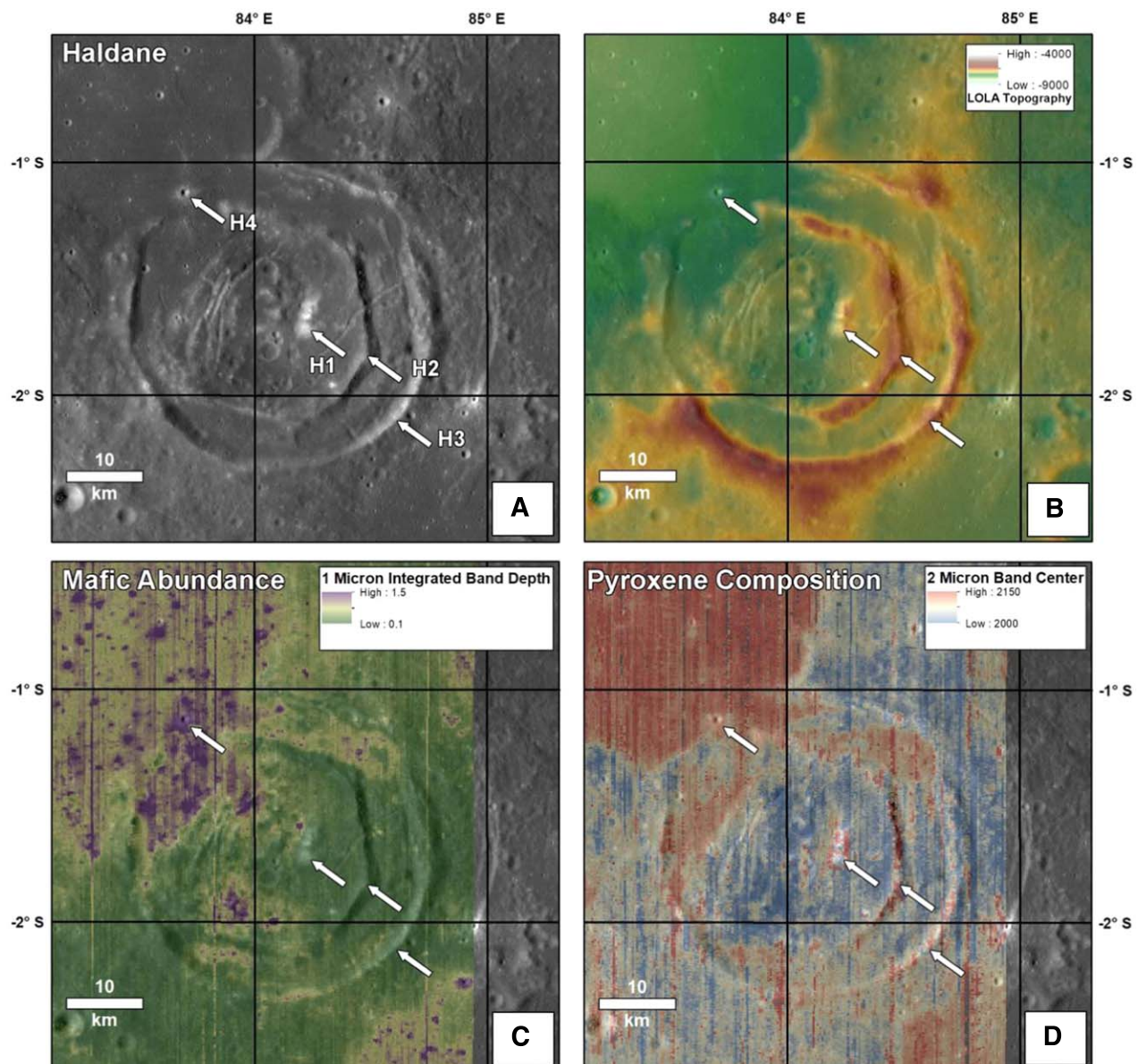
Figure 3. Geological and mineralogical maps for the Haldane crater. (A) LROC WAC imagery (Robinson et al. 2010), (B) LOLA topography (Smith et al. 2010), (C) M3 1 μm integrated band depth (sensitive to mafic mineral abundance), and (D) M3 2 μm band center (Moriarty & Pieters 2016). In general, Mg-rich pyroxenes exhibit short-wavelength 1 μm and 2 μm bands; band centers shift to longer wavelengths with increasing Fe and Ca content (Klima et al. 2007, 2011). Labeled arrows indicate the locations of spectra given in Figure 6.

abundance maps (Lemelin et al. 2016) as well as M^3 spectra and mineralogically sensitive parameter maps (Moriarty & Pieters 2016). Plagioclase is the primary component of the lunar highlands crust, and its distribution therefore serves as a tracer of crustal materials. An overview of the plagioclase abundance across Smythii is given in Figure 2 (Lemelin et al. 2016). Volcanic mare basalts exhibit relatively low plagioclase abundances while feldspathic crustal materials exhibit high plagioclase abundance; plagioclase abundance ranges from 50 to 85 wt%.

Basalt of Mare Smythii floods the inner basin of Smythii, as well as a number of smaller superimposed simple and complex impact craters (mapped as Mare). Mare basalts flood the floor of the Neper crater. Mare Marginis onlaps onto the continuous ejecta of the Neper crater and other degraded lunar highlands material to the north of the Smythii basin. Smaller pools of mare basalt occur within other superposed craters within the

Smythii basin, including Schubert C and Haldane. Patterns of higher reflectance interpreted as lunar swirls (Denevi et al. 2016) occur within both Mare Marginis and Mare Neper.

The basalts of Mare Smythii are interpreted to overlie impact breccia and melt sheet within the inner depression of the Smythii basin. However, the inner depression is superposed by many post-Smythii impact craters, and therefore mixtures of breccia and ejecta from these younger craters have degraded and coated the surface, limiting exposures of Smythii melt. This is also the condition for the zone of splashed melt and breccia within the annulus of the Smythii basin. Therefore, this study identifies complex craters that superpose the Smythii basin and may uplift and expose Smythii impact melt material from depth, discussed next.

The rims and central peaks of Smythii, as well as several other craters across the region (including Neper, Schubert C, and Haldane), exhibit plagioclase abundances greater than 85%
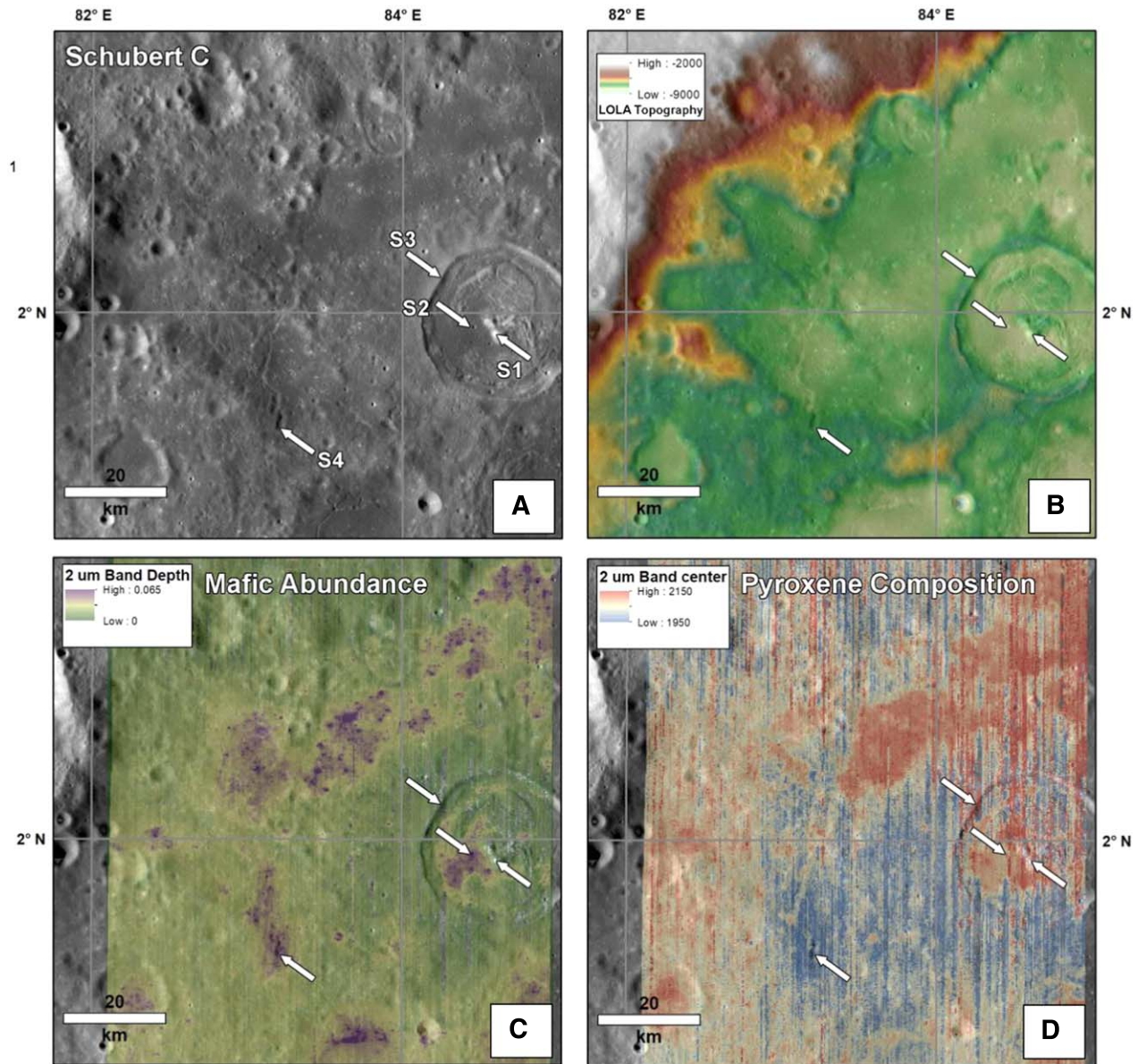
Figure 4. Same as Figure 3 for Schubert C. In (C), the 1 μm integrated band depth has been replaced with a 2 μm band depth, a similar but independent measure of mafic abundance.

(in contrast to ∼35 wt% in the mare), indicating the presence of relatively pure highlands crustal compositions (Figure 2). Neper, Schubert C, and Haldane craters postdate the formation of the Smythii basin and have central peaks, which expose uplifted material; therefore, they have been mapped in greater detail. Stratigraphic uplift depths for each of these craters were estimated using the equation established by Cintala & Grieve (1994, 1998) that relates the final crater diameter to depth of uplift for lunar craters:

$$u_s = 0.022 D_r^{1.45}, \qquad (1)$$

where D_r is the final rim-to-rim diameter and u_s is the depth of uplift. Accordingly, the central peak of Neper (crater diameter c. 140 km) uplifted material from a depth of c. 28.5 km, the central peak of Schubert C (crater diameter c. 31 km) uplifted material from c. 3 km, and the central peak of Haldane (crater diameter c. 41 km) uplifted material from c. 4.5 km.

The Neper crater is superposed onto the annulus of the Smythii basin and, therefore, likely impacted a zone of splashed melt and breccia. While Neper's central peak hosts well-exposed outcrops of bedrock, this material was uplifted from depths below the thickness of Smythii's splash melt and therefore these outcrops are likely Smythii basement material and primarily feldspathic lunar highlands crust, but potentially also upper mantle material (see Wieczorek et al. 2013). Fault scarps along Neper's (primarily northern) wall likely expose Smythii material, Neper breccia, ejecta, slumped material, and also host splashed melt ponds. Therefore, these outcrops cannot be uniquely ascribed to Smythii impact melt with any certainty.

Schubert C (diameter c. 31 km) and Haldane (diameter c. 41 km) are floor-fractured, complex craters located within the central depression of the Smythii basin and their central peaks uplift material from c. 3 km to c. 4.5 km, respectively (mapped as Smythii impact melt), well within the lower bounds of estimates for the thickness of the Smythii melt sheet. Numerous
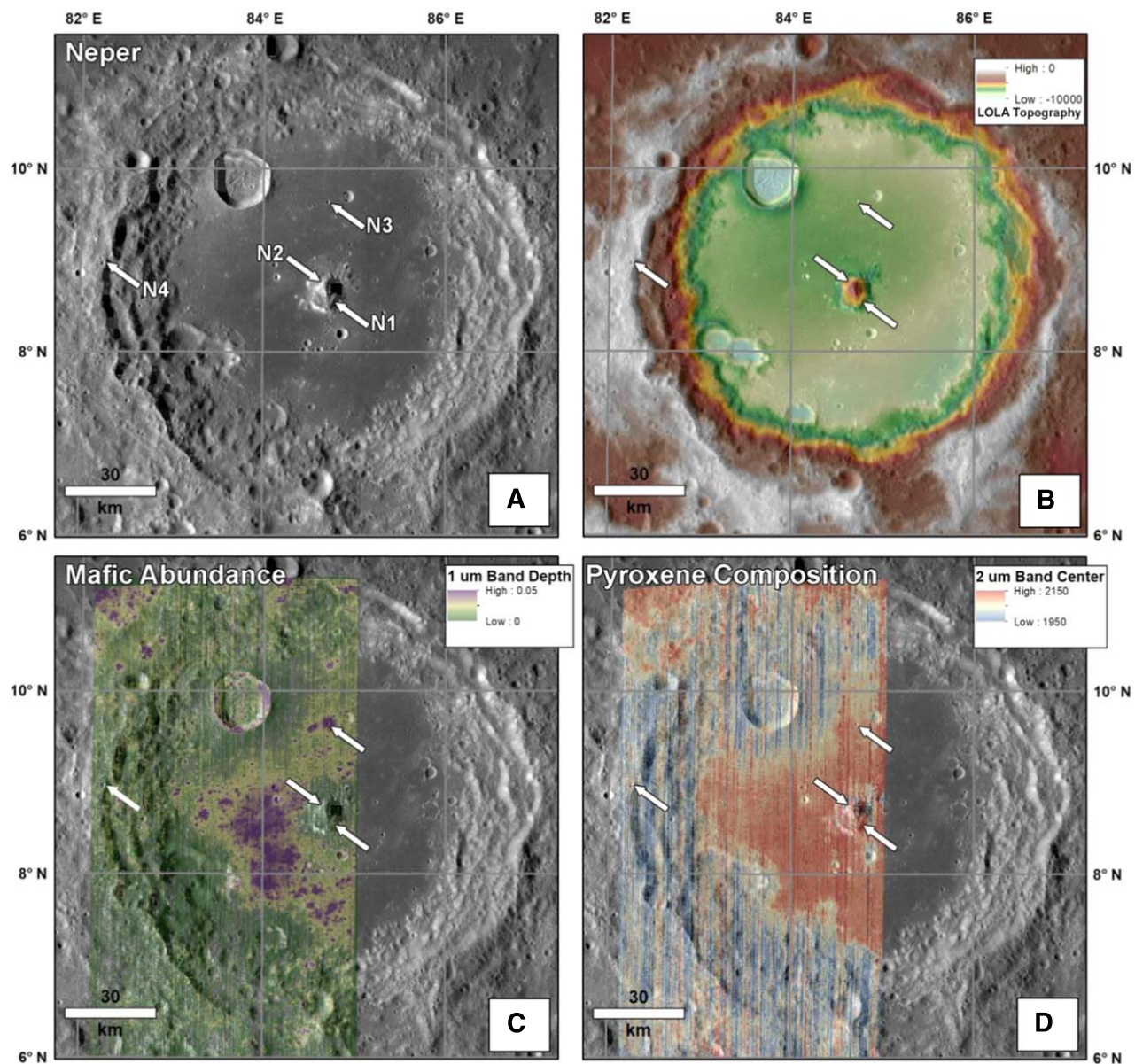
Figure 5. Same as Figure 3 for Neper. In (C), the 1 μm integrated band depth has been replaced with a 1 μm band depth, a similar but independent measure of mafic abundance.

well-exposed outcrops and boulder fields occur on the central peak of Schubert C, which are in situ uplifted material rather than younger cover or ejecta. These are an ideal target for sampling possible impact melt from the underlying the Smythii basin because mass wasting constantly exposes fresh material.

For a more detailed mineralogical analysis, mineralogically sensitive parameter maps were generated from M^3 data, focusing on craters Haldane, Schubert C, and Neper (Figures 3–5). Representative spectra from relevant local features are presented in Figure 6. These parameter maps are discussed in more detail in the following paragraphs.

M^3 data for Haldane are presented in Figure 3. Haldane's central peak (H1), inner ring (H2; likely the result of floor uplift Wichman & Schultz 1995), and rim (H3) all exhibit very low 1 μm integrated absorption-band depths, indicating a very low mafic content. This is confirmed spectrally (Figure 6), as these spectra are "featureless" (i.e., they do not exhibit the absorption bands at 1 and 2 μm characteristic of mafic minerals) and

relatively high reflectance. This is consistent with the high plagioclase abundances indicated in Kaguya data (Figure 2). In contrast, a small crater in the nearby mare (H4) exhibits low reflectance, strong absorption bands, and long-wavelength band centers, indicating the presence of abundant Ca,Fe-bearing pyroxenes.

A similar analysis was conducted for Schubert C (Figure 4). As in Haldane, Schubert C's central peak (S1) and rim (S3) exhibit very low mafic abundances and high reflectance, while a local mare crater appears rich in Ca,Fe-bearing pyroxenes. A nearby pyroclastic deposit (S4) exhibits spectral properties similar to laboratory-measured ilmenite-bearing black beads, which have traditionally been difficult to identify from orbit (Figure 6) (Besse et al. 2014). Specifically, this material exhibits very low albedo, and broad 1 and 2 μm absorption bands with unusual band centers (a very long-wavelength 1 μm band paired with a very short-wavelength 2 μm band) (Moriarty & Pieters 2016).
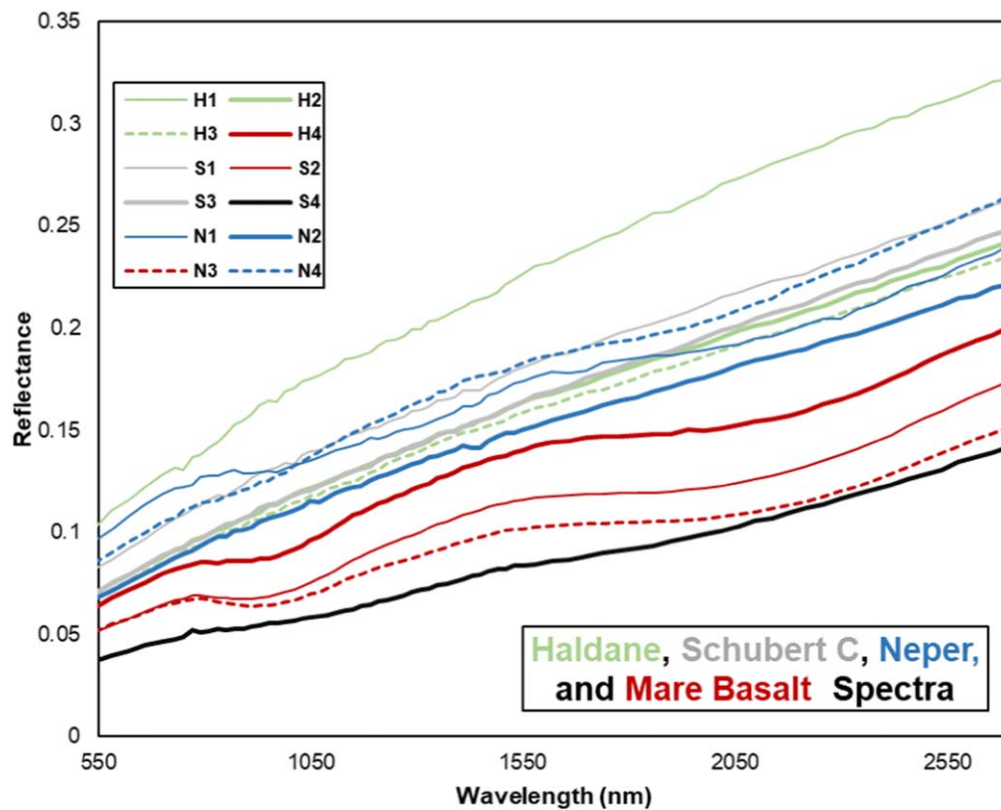
Figure 6. Moon Mineralogy Mapper reflectance spectra from the locations indicated in Figures 3–5. See captions for Figures 3–5 for interpretation of the spectra.

Contrary to Haldane and Schubert C, Neper's central peak exhibits heterogeneity in composition (Figure 5). While much of the peak exhibits low mafic content (N2), a localized outcrop in the southeastern quadrant of the peak exhibits absorption bands near 1 and 2 μm (N1, Figure 6), indicating the presence of a mafic component. Similarly, Neper's wall/rim exhibits 1 and 2 μm absorption bands (N4). Both N4 and N1 exhibit higher reflectance than mare basalts (including the local N3), indicating a higher plagioclase-to-mafic mineral ratio. The absorption bands for materials in Neper's wall/rim (N4) exhibit shorter-wavelength band centers than those in the central peak (N1), indicating a mineral assemblage richer in Mg pyroxenes.

As discussed above, Haldane and Schubert C are thought to excavate through surface mare basalts to excavate rocks from Smythii's impact melt sheet. This is consistent with the compositional patterns observed in Figures 2–5. However, these craters also exhibit some evidence for postformation resurfacing, as they have been embayed, breached, uplifted, and otherwise modified by subsequent volcanic and magmatic activity. However, the highest-standing structures above Smythii's floor (e.g., walls/rims and central peaks) have avoided mare resurfacing and therefore preserve relatively pristine impact materials.

If the inferred stratigraphy is accurate, it implies that the Smythii basin melt sheet is feldspathic in composition. This is somewhat surprising, as inferred impact melt from the nearby, similarly sized Crisium basin exhibits a Mg-pyroxene-bearing mineralogy (Runyon et al. 2020). It is possible that Smythii's melt sheet has sampled shallower, mostly crustal strata, while Crisium melted larger volumes of upper mantle materials due to its slightly larger size and location in the slightly thinner crust (Wieczorek et al. 2013).

Neper is located in Smythii's splash zone and therefore is thought to sample a combination of Smythii ejecta, splashed impact melt, and target crustal material. This is consistent with the observed compositional heterogeneities observed in Neper's central peak and wall/rim, including mixed mafic and feldspathic materials. While datable impact melt from the Smythii-forming impact is likely located here, it is likely mixed with other lithologies.

The geologic map (Figure 7) and compositional data were used for subsurface interpretation of a c. N–S cross section (5× vertical exaggeration), which passes through each of the three investigated superposed complex craters within the Smythii basin (Figure 8). We assume a minimum thickness of the Smythii melt sheet of 6 km within the central depression. Although it could be significantly thicker in places (up to c. 14 km), this allows for a conservative interpretation of where outcrops of this melt sheet may be exposed. A thinner stratigraphic interval of Smythii material (mixed melt, breccia, and ejecta) is interpreted in the annulus outside of Smythii's peak ring.

4. Exploration Concept

We present a brief exploration concept of the central peak of the Schubert C crater (Figure 9) designed to sample inferred Smythii impact melt, interpreted in Figures 7–8. While the traverse map presented could be accomplished by a robotic rover, an astronaut–geologist crew would greatly enhance the exploration timeline, quality of observations, sample quality, and return mass. Option 1: Robotic and/or human assets could land in a saddle in the central peak complex and reach at least six discrete outcrops. Option 2: Assets could land on the smooth, mare-covered crater floor of Schubert C and ascend the
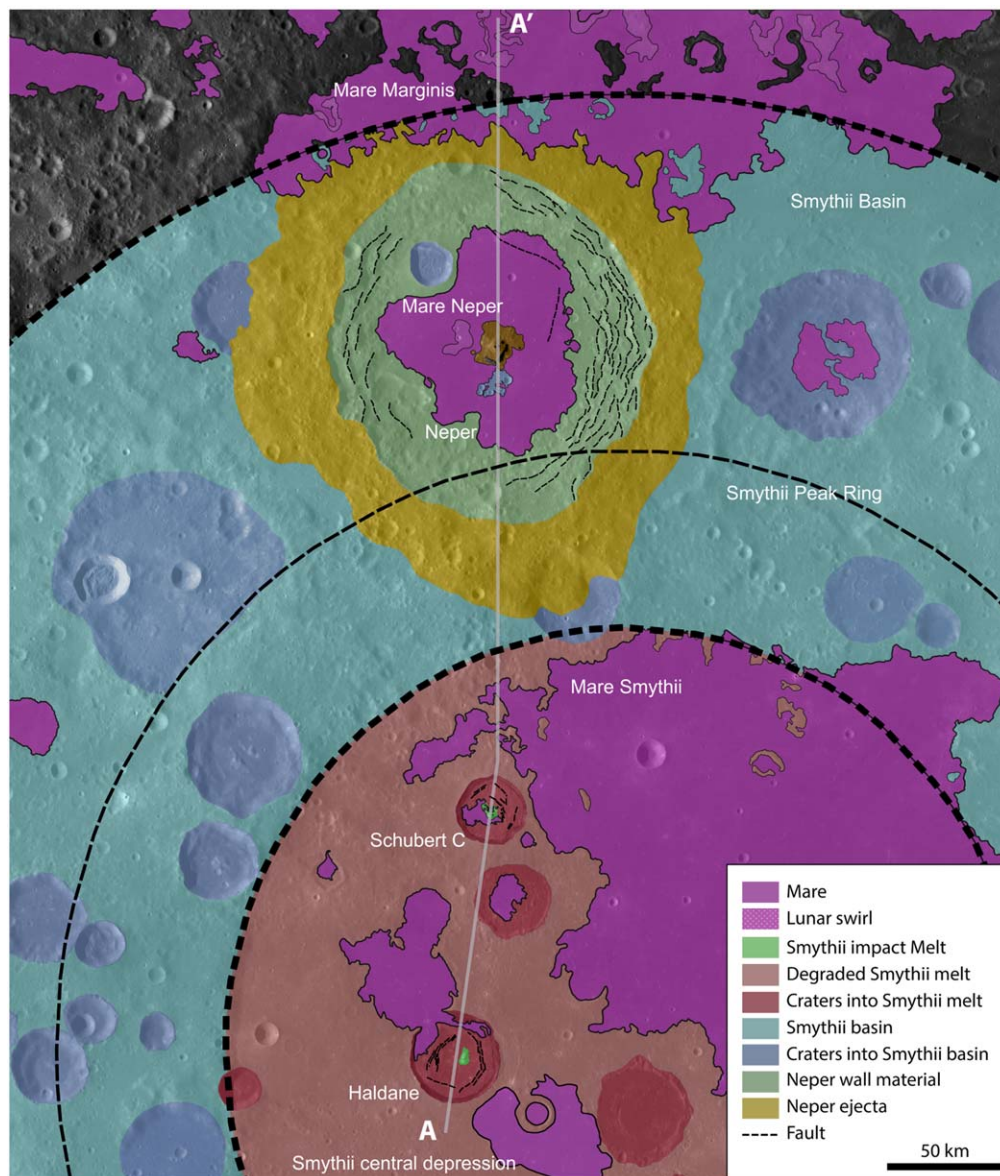
Figure 7. Geologic map of part of the Smythii basin in which we emphasize the Neper, Schubert C, and Haldane craters. The cross-section interpretation of A–A′ is shown in Figure 8. Only craters >20 km diameter were mapped. Mapping does not extend beyond the outer rim of Smythii except for Mare Marginis, which crosses the rim. The base map was projected in QGIS in the equirectangular projection.
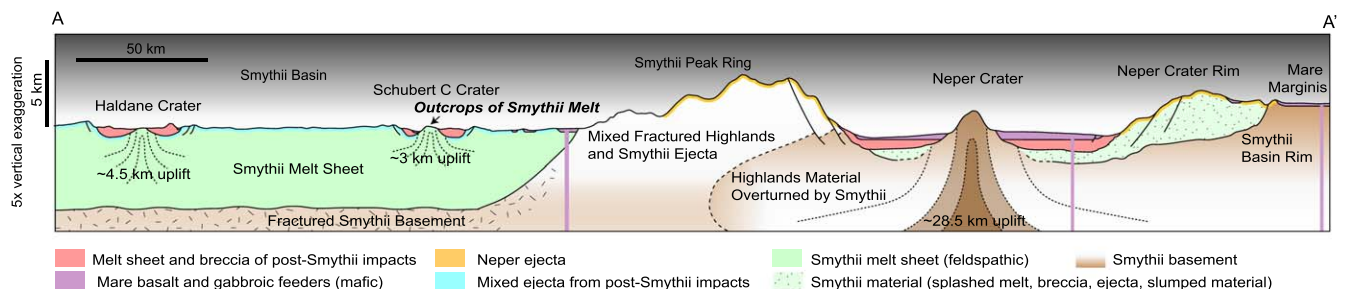

Figure 8. Interpreted subsurface geology of the Smythii basin. Note the central peaks of Schubert C and Haldane craters expose uplifted material of Smythii impact melt. The cross-section line A–A′ is shown in Figure 7. Topography and subsurface are shown at 5× vertical exaggeration.

peak, stopping to select and sample from at least five identified outcrops.

To control for possible hazards related to steep terrain and cliff outcrops, traverses would be limited to navigable slopes of 25° or less for both rovers such as the Space Exploration

Vehicle (Garry & Bleacher 2010) and for astronauts. Sampling from multiple outcrops allows for robust confidence in age determination, either performed in situ (Cohen et al. 2018) or on Earth. A traverse that also samples crater floor material could constrain the flux of objects on the Moon
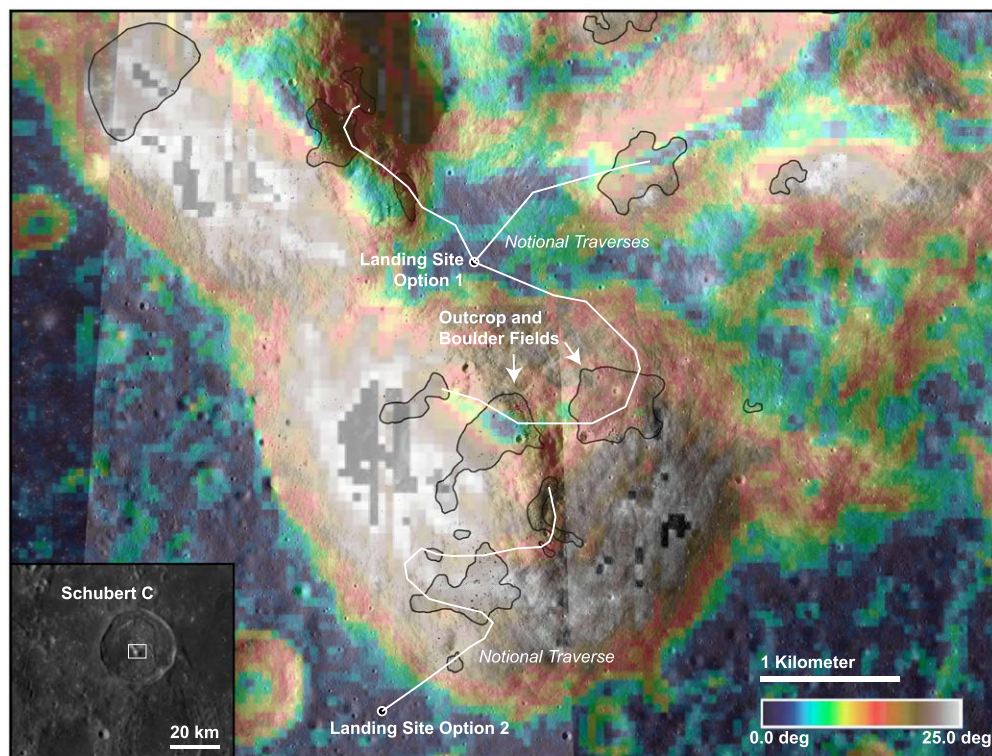
Figure 9. Mission traverse concept for sampling Smythii impact melt on the Schubert C crater central peak. A rover lands on a saddle of the central peak complex or the mare-covered crater floor (near the southwest end of the traverse shown in white) and ascends, sampling boulder and outcrop. This mission could be accomplished by crew or robotically. The slope map in QuickMap is from Barker et al. (2016); slopes greater than 25° shown as gaps in slope data.

forming ∼30 km craters at the time the Schubert C crater formed.

5. Conclusions

Geochronology data from exposures of impact melt that can be confidently linked to the Moon's prominent large basins (>200 km) are necessary to constrain the timing and flux of large impactors during the first 1 Gyr of lunar and terrestrial history and discriminate among differing hypotheses for lunar impactor flux. In this study, a detailed investigation of the Smythii basin (c. 820 km diameter) using photographic, topographic, and compositional data focused on three superposed complex craters, which potentially uplifted Smythii impact melt. Compositional analyses using spectral data, together with stratigraphy and melt-sheet thickness estimates, indicate Smythii's melt sheet is feldspathic in composition, suggesting the Smythii impact sampled primarily crustal material. Our interpretation—encapsulated in a geologic map and geologic cross section (Figures 7–8)—indicates that the central peaks of the Schubert C and Haldane craters likely uplift material from Smythii's impact melt sheet. The Neper crater's central peak likely uplifts basement material that underlies any Smythii material in the splash zone of the basin annulus. Neper's northern rim may expose faulted blocks of Smythii material, but these outcrops may be contaminated by Neper ejecta. We propose that the central peak complex of Schubert C is the best candidate for sampling Smythii impact melt due to (1) its location within the central depression of the Smythii basin, (2) the relative stratigraphic uplift of its central peak in comparison to the inferred thickness of Smythii's continuous melt sheet, and (3) its extensive bedrock outcrops. A mission sent to the well-exposed outcrops of the uplifted

Smythii melt sheet within the southwestern part of Schubert C's central peak complex would enable age determination of Smythii's formation within the broader lunar chronostratigraphic framework.

ORCID iDs

Kirby D. Runyon ⓘ https://orcid.org/0000-0001-6361-6548
Lyle Nelson ⓘ https://orcid.org/0000-0001-5546-0387
Daniel P. Moriarty III ⓘ https://orcid.org/0000-0001-6320-2337

References

Barker, M. K., Mazarico, E., Neumann, G. A., et al. 2016, Icar, 273, 346
Bell, E. A., Boehnke, P., Harrison, T. M., & Mao, W. L. 2015, PNAS, 112, 14518
Besse, S., Sunshine, J., Staid, M., et al. 2013, Icar, 222, 229
Besse, S., Sunshine, J. M., & Gaddis, L. R. 2014, JGRE, 119, 355
Boardman, J. W., Pieters, C. M., Green, R. O., et al. 2011, JGRE, 1161, E00G14
Boehnke, P., & Harrison, T. M. 2016, PNAS, 113, 10802

Bontognali, T. R. R., Sessions, A. L., Allwood, A. C., et al. 2012, PNAS, 109, 15146
Bratt, S. R., Solomon, S. C., Head, J. W., & Thurber, C. H. 1985, JGRB, 90, 3049
Burns, R. G. 1993, Mineralogical Applications of Crystal Field Theory (Cambridge: Cambridge Univ. Press)
Cadogan, P. H., Turner, G., & Massey, H. S. W. 1977, RSPTA, 284, 167
Chapman, C. R., Cohen, B. A., & Grinspoon, D. H. 2007, Icar, 189, 233
Cheek, L. C., Donaldson Hanna, K. L., Pieters, C. M., Head, J. W., & Whitten, J. L. 2013, JGRE, 118, 1805
Cintala, M. J., & Grieve, R. A. F. 1994, in Large Meteorite Impacts and Planetary Evolution, ed. B. O. Dressler, R. A. F. Grieve, & V. L. Sharpton (Boulder, CO: Geological Society of America), 51
Cintala, M. J., & Grieve, R. A. 1998, M&PS, 33, 889
Cohen, B. A., Petro, N. E., Lawrence, S. J., et al. 2018, LPSC, 49, 1029
Denevi, B. W., Robinson, M. S., Boyd, A. K., Blewett, D. T., & Klima, R. L. 2016, Icar, 273, 53
Fassett, C. I., Head, J. W., Kadish, S. J., et al. 2012, JGRE, 117, E00H06
Gillis, J. J., & Spudis, P. D. 2000, JGR, 105, 4217
Garry, W. B., & Bleacher, J. E. 2010, LPSC, 41, 2209
Haskin, L. A. 1998, JGR, 103, 1679
Head, J. W. 1974, Moon, 11, 327
Hiesinger, H., Head, J. W., III, Wolf, U., Jaumann, R., & Neukum, G. 2010, JGRE, 115, E03003
Isaacson, P. J., Pieters, C. M., Besse, S., et al. 2011, JGRE, 116, E00G11
Joyce, G. F. 2002, Natur, 418, 214
Klima, R. L., Dyar, M. D., & Pieters, C. M. 2011, M&PS, 46, 379
Klima, R. L., Pieters, C. M., & Dyar, M. D. 2007, M&PS, 42, 235
Knoll, A. H., Bergmann, K. D., & Strauss, J. V. 2016, RSPTB, 371, 20150493
Kring, D. A., & Cohen, B. A. 2002, JGRE, 107, 5009
Lemelin, M., Lucey, P. G., Gaddis, L. R., Hare, T., & Ohtake, M. 2016, LPSC, 47, 2994
Liu, D., Jolliff, B. L., Zeigler, R. A., et al. 2012, E&PSL, 319, 277
McCollom, T. M., Lollar, B. S., Lacrampe-Couloume, G., & Seewald, J. S. 2010, GeCoA, 74, 2717
Merle, R. E., Nemchin, A. A., Grange, M. L., Whitehouse, M. J., & Pidgeon, R. T. 2014, M&PS, 49, 2241
Michael, G., Basilevsky, A., & Neukum, G. 2018, Icar, 302, 80
Mojzsis, S. J., Arrhenius, G., McKeegan, K. D., et al. 1996, Natur, 384, 55
Morbidelli, A., Marchi, S., Bottke, W. F., & Kring, D. A. 2012, E&PSL, 355, 144
Morbidelli, A., Nesvorny, D., Laurenz, V., et al. 2018, Icar, 305, 262
Moriarty, D. P., III, & Pieters, C. M. 2016, M&PS, 51, 207
Moriarty, D. P., & Petro, N. E. 2020, LPSC, 51, 2660
Morse, Z. R., Osinski, G. R., & Tornabene, L. L. 2018, Icar, 299, 253

Neumann, G. A., Zuber, M. T., Wieczorek, M. A., et al. 2015, SciA, 1, e1500852
National Research Council 2007, The Scientific Context for Exploration of the Moon, Academy of Sciences (Washington, DC: The National Academies Press), https://doi.org/10.17226/11954
Norman, M. D., Duncan, R. A., & Huard, J. J. 2010, GeCoA, 74, 763
Orgel, C., Michael, G., & Fassett, C. I. 2018, JGRE, 123, 748
Osinski, G. R., Tornabene, L. L., & Grieve, R. A. 2011, E&PSL, 310, 167
Pearce, B. K., Tupper, A. S., Pudritz, R. E., & Higgs, P. G. 2018, AsBio, 18, 343
Pieters, C. M., Boardman, J., Buratti, B., et al. 2009, CSci, 96, 500, http://www.jstor.org/stable/24105459
Pieters, C. M., Hanna, K. D., Cheek, L., et al. 2014, AmMin, 99, 1893
Robinson, M. S., Brylow, S. M., Tschimmel, M., et al. 2010, SSRv, 150, 81
Rosing, M. T. 1999, Sci, 283, 674
Runyon, K. D., Moriarty, D. P., III, Denevi, B. W., et al. 2020, JGRE, 125, e06024
Scholten, F., Oberst, J., Matz, K. D., et al. 2012, JGRE, 117, E00H17
Smith, D. E., Zuber, M. T., Neumann, G. A., et al. 2010, GeoRL, 37, L18204
Spudis, P. D., Wilhelms, D. E., & Robinson, M. S. 2011, JGRE, 116, E00H03
Spudis, P. D., Martin, D. J., & Kramer, G. 2014, JGRE, 119, 19
Stettler, A., & Albarede, F. 1978, E&PSL, 38, 401
Swindle, T. D., Spudis, P. D., Taylor, G. J., et al. 1991, LPSC, 21, 167
Tera, F., Papanastassiou, D. A., & Wasserburg, G. J. 1974, E&PSL, 22, 1
Tice, M. M., & Lowe, D. R. 2006, ESRv, 76, 259
van der Bogert, C. H., Hiesinger, H., & Spudis, S. 2017, LPICo, 1988, 6009
van Kranendonk, M. J., Webb, G. E., & Kamber, B. S. 2003, Geobiology, 1, 91
Vaughan, W. M., Head, J. W., Wilson, L., & Hess, P. C. 2013, Icar, 223, 749
Warren, P. H. 2003, in The Moon, ed. H. D. Holland & K. K. Turekian, Vol 1 (New York: Elsevier), 559
Wichman, R. W., & Schultz, P. H. 1995, JGR, 100, 21201
Wieczorek, M. A., Neumann, G. A., Nimmo, F., et al. 2013, Sci, 339, 671
Wilhelms, D. E., & El-Baz, F. 1977, LPICo, 304, 200
Wilhelms, D. E., & McCauley, J. F. 1971, Geologic map of the near side of the Moon. USGS Investigation Series Map I-703, http://roussev.net/sdhash/tutorial-data/files/904.pdf
Wilhelms, D. E., McCauley, J. F., & Trask, N. J. 1987, The Geologic History of the Moon (Denver, CO: US Geological Survey)
Wilson, L., & Head, J. W. 2011, LPSC, 42, 1345
Yingst, R. A., & Head, J. W., III 1998, JGRE, 103, 11135
Young, K. E., Evans, C. M., Hodges, K. V., Bleacher, J. E., & Graff, T. G. 2016, ApGC, 72, 77
Young, K. E., van Soest, M. C., Hodges, K. V., et al. 2013, GeoRL, 40, 3836
Zuber, M. T., Smith, D. E., Neumann, G. A., et al. 2016, Sci, 354, 438